



# Imaging hair cells through laser-ablated cochlear bone

**MARILISA ROMITO,<sup>1,\*</sup> YE PU,<sup>1</sup> KONSTANTINA M. STANKOVIC,<sup>2</sup> AND DEMETRI PSALTIS<sup>1</sup>**

<sup>1</sup>*Optics Laboratory, School of Engineering, Ecole Polytechnique Fédérale de Lausanne (EPFL), 1015 Lausanne, Switzerland*

<sup>2</sup>*Department of Otolaryngology – Head and Neck Surgery, Harvard Medical School and Massachusetts Eye and Ear, Boston, MA 02114, USA*

\*[marilisa.romito@epfl.ch](mailto:marilisa.romito@epfl.ch)

**Abstract:** We report an innovative technique for the visualization of cells through an overlying scattering medium by combining femtosecond laser bone ablation and two-photon excitation fluorescence (TPEF) microscopy. We demonstrate the technique by imaging hair cells in an intact mouse cochlea *ex vivo*. Intracochlear imaging is important for the assessment of hearing disorders. However, the small size of the cochlea and its encasement in the densest bone in the body present challenging obstacles, preventing the visualization of the intracochlear microanatomy using standard clinical imaging modalities. The controlled laser ablation reduces the optical scattering of the cochlear bone while the TPEF allows visualization of individual cells behind the bone. We implemented optical coherence tomography (OCT) simultaneously with the laser ablation to enhance the precision of the ablation and prevent inadvertent damage to the cells behind the bone.

© 2019 Optical Society of America under the terms of the [OSA Open Access Publishing Agreement](#)

## 1. Introduction

Seeing through scattering media is one of the major challenges for optical imaging. An emerging class of wave front shaping techniques undoes the distortion due to scattering through a carefully shaped wave front [1–3]. By sending such a shaped wave front back through the same medium, the scattering can be unscrambled and the original incident wave front is recovered. This can be used to produce a laser focus behind the scattering medium [4,5], which can be scanned for imaging via the correlation in the scattered wave front (memory effect) [6]. Variations of these techniques have been applied in brain imaging *in vitro* [7] and *in vivo* [8]. However, great challenges remain for obtaining access from both sides of the scattering layer [9], or placing proper beacons in the target region [1].

In this paper, we explore an alternative method that involves the creation of artificial windows in scattering media by thinning them down to a thickness approximately equal to one photon mean free path (MFP) using femtosecond laser ablation. We demonstrate for the first time transosseous imaging in an intact extracted mouse cochlea by thinning the encasing bone to enable visualization of cochlear cells through the thinned scattering bone using ballistic photons. Bone thinning has been used before for brain imaging in live animals [10,11]. Owing to the nonthermal process and the highly confined ablated region, ultrafast laser pulses are used to perform very precise cutting of materials in manufacturing [12], and have been used in microsurgery, such as cutting of specimens ranging from subcellular organelles to large bones [13]. We implemented a simultaneous OCT imaging system to allow measurement of the bone thickness and prevent unintentional damage to the cells behind the bone. Optical coherence tomography has been used previously in laser ablation for monitoring and guidance [14,15], and femtosecond laser osteotomy has been recently employed to enable two-photon transcranial imaging in mice [16]. The novelty of our work is the application of OCT-guided femtosecond laser ablation in an intact

cochlea for precise bone thinning without breaching it to achieve TPEF imaging of hair cells (HCs) through the ablated bone.

The cochlea is a spiral-shaped part of the inner ear responsible for mechanoelectric transduction of sound waves into electrical signals transmitted to the brain. It hosts the HCs, which are part of the organ of Corti (OC), and are the sensory receptors of the auditory system. HCs transform the incoming energy of sound waves into electrical signals that lead to neurotransmitter release and excitation of the cochlear nerve. The majority of hearing loss originates from the cochlea, and this ailment is known as sensorineural hearing loss (SNHL). Although damage of any cochlear cell type can cause SNHL, HCs and cochlear neurons are frequently damaged in many genetic and environmentally-induced types of hearing loss [17,18]. Therefore, imaging the inner ear's microanatomy is of high interest for the study and therapy of hearing loss. Therapies for SNHL are currently essentially limited to prosthetic devices (hearing aids and cochlear implants); however, promising emerging approaches include localized inner-ear delivery of correct genes, gene editing reagents, small molecules and stem cells [19–22]. It is essential that diagnostic methods of the cellular cause of SNHL be developed to select among the emerging therapeutic options.

The primary challenge preventing the visualization of the intracochlear microanatomy is scattering by the surrounding bone, which strongly limits the focusing capability of an imaging system as well as the collection efficiency of the generated optical signal. Furthermore, intracochlear imaging is particularly difficult because of the small dimensions of the cochlear chambers, their complex spiraling structure and the difficulty of tool access. Impressive results were obtained with optical coherent tomography (OCT) for *in vivo* imaging of the cochlea in animal models, but the achieved resolution was limited (8.7  $\mu\text{m}$  axially and 9.8  $\mu\text{m}$  laterally [23,24]). To improve the spatial resolution of conventional OCT, micro-optical coherence tomography ( $\mu\text{-OCT}$ ) was utilized to resolve cochlear microanatomy at a cellular level in *ex vivo* intact guinea pigs cochleae [25]. Nevertheless, additional efforts are required to improve both penetration depth and resolution. In other studies [26–28], specific optical clearing protocols were utilized to increase bone transparency and acquire high-resolution fluorescence images through the whole volume of the cochlea. However, optical clearing treatments may irreversibly modify the mechanical properties of the bone, and may be ototoxic and cause hearing loss. Additional methods for cochlear visualization are magnetic resonance imaging (MRI), computed tomography (CT) and micro-CT ( $\mu\text{CT}$ ). Although MRI and CT are noninvasive clinical tools, they do not have the resolution to identify cochlear microanatomy [29]. Micro-CT has been used to create a three-dimensional (3D) model of the cochlear bone [30,31] and fluid chambers (when using osmium tetroxide as contrast agent for soft tissues [32]). Recently, synchrotron-radiation phase contrast imaging (SR-PCI) has been applied to human 3D intact temporal bones to resolve cellular structure within the inner ear [29]. However, the high dose of radiation used in  $\mu\text{CT}$  and SR-PCI studies prevent immediate translation of these techniques to living humans.

Modern optical microscopy techniques are being applied to excised OC to better understand hearing loss. Two-photon excitation fluorescence (TPEF) microscopy [33,34] in particular has been of interest lately for intracochlear imaging. Yang et al. [35] reported TPEF imaging of the mouse HCs without OC extraction, exogenous dyes or drilling through the cochlear bone. HCs were imaged through the membranous round window using a near-infrared femtosecond laser as the excitation and endogenous TPEF and second harmonic generation as the contrast mechanisms. Although the region of the OC accessible through the round window is the most likely place for the initiation of the sensorineural damage, restricting imaging to this region limits the diagnostic field of view. This motivated us to demonstrate the laser ablation method by creating alternative access pathways through the cochlear bone.

The inner ear uniquely suits the technique we describe in this paper. The 3D, spiraling, bony labyrinth of the cochlea has so far presented an insurmountable challenge for cellular-level

diagnostics needed for the treatment of many hearing diseases. This dense, relatively acellular bone lacks the vascular diploic space [36]. Therefore, bleeding should not be an issue in the process of non-thermal ablation. Furthermore, owing to the small dimension of the cochlea, only a minute amount of bone is removed in order to achieve cellular-level imaging of the organ of Corti, requiring low ablation power and causing insignificant impact from the laser-induced shock wave and heat. In this work, the volume of bone needed to be removed through ablation was on the order of  $(150\ \mu\text{m})^3$ , or  $0.0034\ \text{mm}^3$ , ablated at a rate of  $0.01\text{--}0.05\ \text{mm}^3\ \text{min}^{-1}$  depending on the fluence used and the properties of the bone. In the human cochlea, we expect the ablation area and depth to be roughly twice as large, giving an ablation volume of  $0.027\ \text{mm}^3$ .

## 2. Methods

### 2.1. Experimental setup

The experimental setup is shown in Fig. 1. For ablation, we used a compact femtosecond pulsed fiber laser source (Satsuma HP2, Amplitude Systems) with a center wavelength at 1030 nm, an average output power of 20W, and tunable pulse width, repetition rate and pulse energy. The laser source integrates a kilohertz regenerative amplifier with a maximum pulse energy of 40  $\mu\text{J}$  at a minimum pulse duration of 300 fs, which is required for ablation. To quantify the volume ablation rate under laser irradiation and the sample thickness, we combined the ultrafast laser ablation setup with a spectral-domain OCT imaging system (Ganymede II, Thorlabs) working at a center wavelength of 930 nm. The OCT imaging allows the thickness of the targeted sample area to be monitored during ablation. Forty-seven percent of the laser energy is delivered from the ablation laser to the OCT objective, the transmittance of which is 87% at the ablation wavelength. The overall energy delivery efficiency is thus roughly 40% in the combined system. As shown in Fig. 1(a), the femtosecond laser beam was expanded, collimated and directed into the head of the OCT system. We integrated the OCT measurement beam with the ablation beam via a beamsplitter to monitor the target area. The two beams were scanned simultaneously on the sample by controlling the galvanometric mirrors inside the OCT head via a Labview interface (Fig. 1(b)). No further synchronization was used between the ablation laser pulses and the OCT scanner. The OCT head also includes a camera providing a BF top view of the scanned area, which helps locate the ablation area. The BF imaging feedback is complemented with OCT images of the sample before and after laser ablation.

In all experiments, the ablation scan was carried out at a constant rate. Under the control of the OCT scanner, the ablation beam moves at  $7.5\ \text{mm}\ \text{s}^{-1}$ , with the focal spot (Airy disk) of roughly  $12.5\ \mu\text{m}$  diameter moving  $1.5\ \mu\text{m}$  every pulse. Thus, each adjacent spot overlaps with the previous one by nearly 92%. Each scan line also moves  $1.5\ \mu\text{m}$  farther down from the previous line. On average, each point in an ablation area receives roughly 28 ablation pulses during each two-dimensional scan.

We acquired TPEF images of the whole mounts with an overlying cochlear bone layer (Fig. 2). The cochlear bone was laser ablated down to different thicknesses, placed on top of the whole mount sample (covered with a #1 microscope coverslip) and glued at one edge for stability (Fig. 2(a)). This specific geometry was selected to reproduce the range of anatomically accurate distances between the OC and the inner wall of the cochlear bone in mice, which can measure up to  $300\ \mu\text{m}$  depending on the relative OC topology. Assuming the optical properties of the intracochlear fluid comparable to those of water, an optical path of  $200\ \mu\text{m}$  in the intracochlear fluid can be reproduced with a  $160\ \mu\text{m}$  in glass, which is similar to a #1 coverslip. The TPEF signals are collected in an epi configuration through the microscope objective, passing again through the bone before being detected (Fig. 2(b)).

The mounted samples were imaged with a Leica SP5 multiphoton microscope system equipped with a tunable mode-locked Ti:Sapphire laser (Coherent Chameleon Ultra II, pulse width 140 fs) as the light source. The excitation wavelength was set at 785 nm when using Rhodamine 6G as

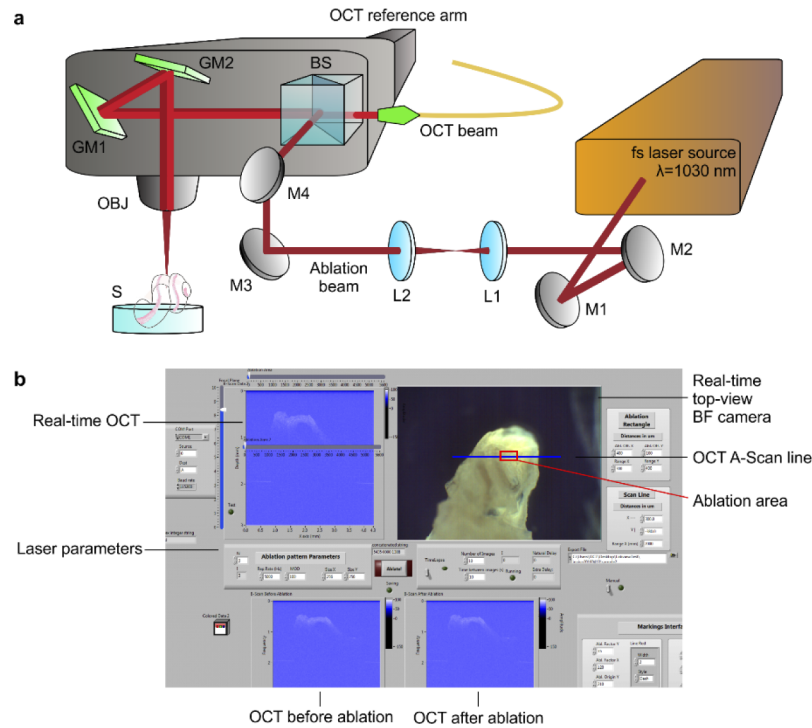


**Fig. 1.** Experimental setup for ultrafast laser ablation of cochlear bone. **(a)** Laser ablation setup combined with the OCT system. The ablation beam is expanded, collimated and directed into the OCT head. After the beamsplitter (BS), both OCT beam and ablation beam reach a pair of galvanometric mirrors (GM1 and GM2) and are then redirected toward the focusing objective (OBJ) onto the sample (S). L1 and L2, lenses. M1-M4, mirrors. **(b)** User interface for the control of laser ablation. The interface allows the control of simultaneous real time OCT and BF imaging systems, the choice of the laser parameters for ablation, the selection of the targeted area and the OCT imaging comparison of the sample before and after ablation.

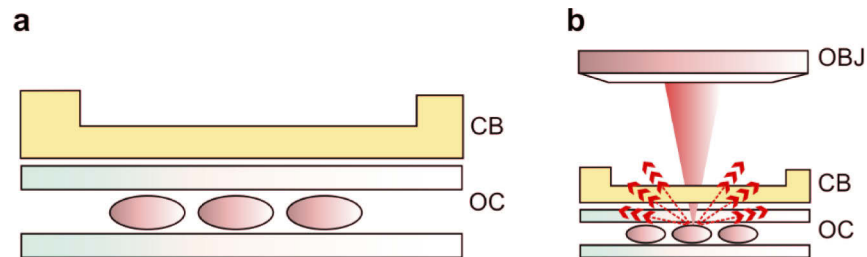


**Fig. 2.** Preparation of a whole mount sample covered with a bony chip for TPEF efficiency studies. **(a)** Sectional sketch of the sample. The whole mount includes a fixed OC stained with Rhodamine 6G and placed between two microscope slides (in blue). The bony chip varies in thickness (based on precise laser ablation) and is placed on the coverslipped whole mount. **(b)** Schematic of the light transmission through cochlear bone. Depending on bone thickness, a certain amount of light will excite the OC and a fraction of emitted light will be collected back for imaging. CB, cochlear bone. OC, organ of Corti. OBJ, objective.

the fluorescent staining, and at 920 nm when using Phalloidin 488 to visualize F-actin. The TPEF signals were excited and collected through a Leica HCX APO 20× 1.0 NA water immersion microscope objective in an epi configuration. After a 680 nm shortpass filter to eliminate the excitation light, the signal was sent to a photomultiplier tube (PMT) for detection through a bandpass filter centered at 525 nm (50 nm bandwidth). The maximum average excitation power measured at the focal plane was ~10 mW, resulting in a peak intensity of approximately  $4.6 \times 10^{10} \text{ W cm}^{-2}$  and  $3.4 \times 10^{10} \text{ W cm}^{-2}$  for the wavelength of 785 nm and 920 nm, respectively. For all images, intensities were averaged over 48 consecutive scanning frames.

TPEF images of intact OC through the ablated intact cochlear bone were acquired using the same Leica SP5 multiphoton microscope system described above.

## 2.2. Sample preparation

Mice were sacrificed and inner ears were extracted (Fig. 3). The cochleae were gently perfused with cold 4% paraformaldehyde in 0.1 M phosphate-buffered saline (PBS) and post-fixed in 4% paraformaldehyde for at least 2 hours at room temperature. The coiled murine cochlea was approximately 5 mm long (Fig. 3(a)), spiraling two turns around the central axis. The OC extends along the length of the cochlea, as schematized in Fig. 3(b), depicting the spiraling OC encased by cochlear bone with two apertures: the round window (RW) and the oval window (OW).

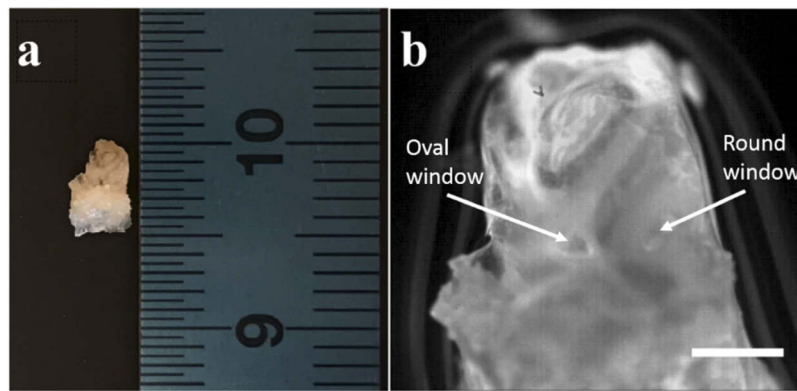


**Fig. 3.** Dissection of a murine cochlea. (a) Photograph of an extracted murine inner ear. (b) Image of the cochlea as viewed using the integrated BF microscope in the OCT system. Anatomic details are clearly visible. Arrows point to the natural windows (round and oval windows) in the cochlea. Scale bar: 1 mm.

To prepare whole mount samples, the cochlear bone was removed, the OC was microdissected, permeabilized with 0.25% Triton-X 100 for 15 minutes on a shaker, immersed in a 0.02% rhodamine 6G (ACROS) in PBS for two minutes, and washed three times in PBS for five minutes each. The stained sample was mounted in a mounting medium (ProLong Diamond from Life Sciences Technologies) and coverslipped.

To prepare 3D intact cochlear samples, the fixed cochleae were permeabilized with 0.25% Triton-X 100 for 15 minutes on a shaker, immersed in a phalloidin solution (diluted 1:200 in PBS from a 6.6  $\mu\text{M}$  stock solution in methanol) and rinsed three times in cold PBS for five minutes each on a shaker. To improve the stability and allow an optimal orientation angle for ablation and imaging, the stained intact cochleae were mounted in a mold made of 1% agarose in water, and oriented with the ablated bone area facing the microscope objective.



### 2.3. Animal experiments

All animal experiments were performed following the national and institutional guidelines for the care and use of laboratory animals, with the approval of Ecole Polytechnique Fédérale de Lausanne (EPFL). Ten seven-week old mice (NMRI strain) were used in this study. The mice were sacrificed by an intraperitoneal injection of pentobarbital at a concentration of 150mg/kg (Esconarkon, concentration 150 mg/ml) prior to decapitation and inner ear extraction.

## 3. Results

### 3.1. Femtosecond laser ablation of murine cochlear bone and TPEF microscopy of OC through the ablated bone

As an initial calibration step, we ablated pieces of mouse cochlear bone. We used a compact 1030 nm, 20W femtosecond fiber laser (Satsuma HP2, Amplitude Systems) with a tunable pulse width, repetition rate, and pulse energy. The laser ablation setup was integrated with a simultaneous OCT system and a bright-field (BF) camera to provide real-time images of the sample (see Methods). After selecting the specimen area to ablate in the transverse plane, OCT images were acquired before and after each laser ablation process to monitor the ablation depth. The focal plane was then moved a certain feeding distance further into the bone and a second round of ablation was carried out. By repeating the procedure several times, we achieved an ablation depth required for TPEF imaging through the bone. For parameter optimization, we investigated the effects of pulse energy, and thus fluence, on the bone ablation while maintaining a pulse width of 330 fs and a repetition rate of 5 kHz throughout this work. The ablation was performed at a numerical aperture (NA) of 0.1, with a pulse fluence ranging from 1.0 to 4.5 J cm<sup>-2</sup>, approximately 1.3–6 times the fluence threshold of 0.5–0.8 J cm<sup>-2</sup> suggested in previous work [37–39]. We did not specifically quantify the fluence threshold in the cochlear bone, although the lowest fluence of 1 J cm<sup>-2</sup> with OCT-detectable ablation depth is reasonably close to the published range.

Results of the femtosecond laser ablation in cochlear bone are shown in Fig. 4. Figure 4(a) shows a representative top view BF image of a cochlear bone sample ablated at a pulse energy of 3.7 μJ delivered on the sample, which corresponds to a pulse fluence of 4.5 J cm<sup>-2</sup>, approximately 6 times the fluence threshold. The ablated area is a square 150 μm x 150 μm pattern formed by raster-scanning the ablation laser focus point-by-point in the area. The scanning was completed in 2 s, during which a total laser energy of 37 mJ was deposited over the ablation area. The yellow dashed line indicates the location of the corresponding OCT image. The OCT sectional views before (Fig. 4(b)) and after (Fig. 4(c)) the ablation reveal precise bone removal, with perpendicular walls, a flat floor surface, and no signs of melting or carbonization.

The quantitative rate of ablation in terms of ablation depth  $\delta$  is summarized in Fig. 4(d) and 4(e). Typically, several rounds of ablation are needed with a laser focus progressively fed into the bone. Other than the initial focusing, a constant feeding step without refocusing is a more feasible approach than refocusing the laser on the ablation surface before the next round. We therefore measured the rate of ablation in a single round as a function of pulse energy for several focal positions below the flat ablation surface formed *a priori*, which is shown in colored symbols in Fig. 4(d). As in the previous example, each ablation round is completed in 2 s. The ensemble average and standard deviation for all rates at different depth reflects the practical rate achievable and its range of variation when the focus depth is not accurately known, which is plotted in black solid symbols with error bars. The multi-round ablation depth as a function of the number of rounds of ablation for various pulse energy is shown in Fig. 4(e), where the shaded region suggests the range of ablation achievable. Given the thickness of the cochlear bone cage, we estimate that no more than 5 rounds of ablation are sufficient to achieve the required ablation depth, which will be completed in about 10 s. Future applications in live sample would have to consider further challenges, such as motion due to breathing and heartbeat, which could compromise the precision

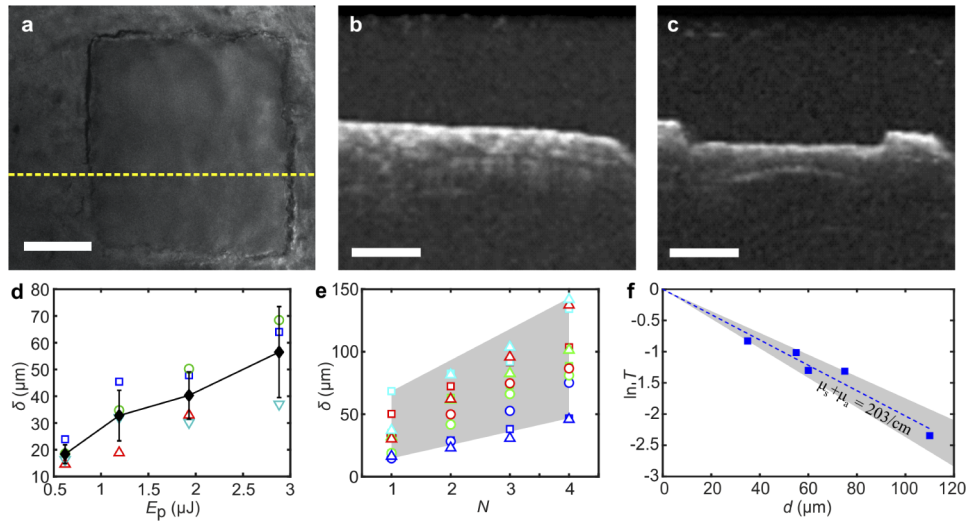


**Fig. 4.** Ultrafast laser ablation of murine cochlear bone. (a) Bright-field view of the ablated bone area ( $150 \times 150 \mu\text{m}^2$ ). (b) A-scan OCT of the bone sample along the yellow dashed line in (a) before ablation. (c) A-scan OCT of the bone sample along the yellow dashed line in (a) after ablation. Scale bars:  $50 \mu\text{m}$ . (d) Single-round ablation depth (rate of ablation) as a function of pulse energy delivered to the sample at various focal positions. Blue squares, laser focus is on the bone surface. Green circles, laser focus is  $5 \mu\text{m}$  into the bone surface. Red triangles, laser focus is  $10 \mu\text{m}$  into the bone surface. Cyan triangles, laser focus is  $20 \mu\text{m}$  into the bone surface. Black solid diamonds, average rate of ablation. Error bars represent one standard deviation. Black line is a visual aide. (e) Ablation depth as a function of rounds of ablation at constant feeding steps of the laser focus. Colors represent pulse energy used. Blue,  $0.82 \mu\text{J}$ . Green,  $1.3 \mu\text{J}$ . Red,  $2.0 \mu\text{J}$ . Cyan,  $2.8 \mu\text{J}$ . Symbols represent feeding step size. Squares,  $5 \mu\text{m}$ . Circles,  $10 \mu\text{m}$ . Triangles,  $20 \mu\text{m}$ . Gray shaded region shows range of ablation depth practically achievable. (f) Measurements of the optical properties of bone based on ablation-controlled thickness. The combined scattering and absorption coefficient is  $203 \text{ cm}^{-1}$ , which are not separated. Gray shaded region suggests the possible range of variations among different samples.

of the ablation at microscale. Such motions, however, could be minimized through the use of general anesthesia and muscle relaxant.

Based on the ablation-controlled bone thickness, we measured the transmission of focused light through the cochlear bone by focusing a weak laser beam of  $1030 \text{ nm}$  wavelength from the ablation laser with a  $10\times$  microscope objective ( $0.25 \text{ NA}$ ) at a position behind the sample. Within the thicknesses considered in this experiment, a significant amount of ballistic photons survives, and a clear focus could be identified when imaged with a  $20\times$  microscope objective ( $0.4 \text{ NA}$ ). This allowed measurement of the ballistic photon intensity through the peak intensity of the laser focus in the well-resolved digital image of the focal spot at a pixel resolution of  $0.26 \mu\text{m}$ . In this regime, contributions from scattered light at the focal spot can be neglected, and the Lambert–Beer law holds for both scattering and absorption as  $I_f = I_0 \exp[-(\mu_s + \mu_a)d]$ , where  $I_f$  is the measured peak focal intensity,  $I_0$  is the focal intensity without attenuation,  $\mu_s$  is the scattering coefficient,  $\mu_a$  is the absorption coefficient, and  $d$  is the sample thickness. The transmissivity is then  $T = I_f / I_0$ . Five samples, each from a different cochlea, ablated to different thicknesses, were measured this way. In order to avoid errors due to Fresnel reflections at several interfaces, we did not use  $I_0$  in this measurement. To estimate the optical coefficients from the measurements, a linear regression in  $\ln T = \ln I_f - \ln I_0$  was used to extract  $\mu_s + \mu_a$  and  $\ln I_0$ , as shown in in Fig. 4(f). We found

that the combined scattering and absorption coefficient  $\mu_s + \mu_a = 203 \text{ cm}^{-1}$  on average at the wavelength ( $1.03 \text{ }\mu\text{m}$ ) involved, which varied from sample to sample in the range of  $175\text{--}237 \text{ cm}^{-1}$ . This value corresponds to a photon mean free path (MFP) of  $49 \text{ }\mu\text{m}$  and is in a good agreement with previous reports [40]. This relatively narrow range of variability suggests that the thickness was well controlled in the ablation. In this measurement, we did not separate the two coefficients because in bones in general [41,42], and in the cochlear bone specifically [40],  $\mu_a$  is at least one order of magnitude smaller than  $\mu_s$ . Furthermore, we did not measure scattering anisotropy because our goal is to ablate the cochlear bone down to one MFP for ballistic photon imaging.

Having characterized the scattering properties of the cochlear bone with ablation-controlled thicknesses, we studied the quality of two-photon imaging through such bone. Of primary importance for imaging, we studied the evolution of the laser focal intensity distribution over bone thickness, which is directly linked to the TPEF imaging point spread function (PSF). In a similar approach to the measurement of the scattering coefficient, we generated a laser focus by focusing a collimated laser beam with a microscope objective ( $0.25 \text{ NA}$ ) through a piece of bone ablated to a specific thickness and placed it close to the objective. The focus spot was then imaged with another microscope objective placed on the opposite side of the bone piece onto a digital camera. Instances of the focal intensity line profile after transmitting through different bone thicknesses are shown in Fig. 5(a), where insets show the corresponding two-dimensional intensity map. A relatively consistent laser focus can be obtained through a bone thickness up to  $75 \text{ }\mu\text{m}$  despite the reduced intensity and the appearance of speckles near the focus for the thicker samples. The intensity profiles of the central peak are similar up to this thickness, suggesting that ballistic photons remain dominant. At a thickness of  $110 \text{ }\mu\text{m}$ , the laser focus is significantly broadened, with substantially lower intensity and severe speckles. This is the point where ballistic photon intensity falls below low-angle scattered (or “snaky”) photons [43]. Beyond this point, the focus spot becomes more and more broadened but remains identifiable owing to the anisotropic (forward) scattering of the bone tissue up to the transport MFP. The temporal profile of the laser pulse also suffers severe broadening in this regime, further reducing the peak intensity. As TPEF emission scales with the square of the excitation intensity, it requires significantly higher laser power to achieve sufficient signal strength through a thicker bone layer. This highlights the importance of thinning the cochlear bone close or below one MFP in thickness to achieve useful TPEF imaging performance.

To investigate the feasibility of TPEF imaging at the cellular resolution required for inner ear diagnostics, we glued each of the ablated bones on top of a different mouse cochlear whole mounts (flat preparation of a microdissected organ of Corti) and performed TPEF microscopy in a commercial multiphoton microscope (Leica SP5). We ablated cochlear bone chips down to different thicknesses, ranging from  $60 \text{ }\mu\text{m}$  to  $100 \text{ }\mu\text{m}$ . We also used a non-ablated bone of  $250 \text{ }\mu\text{m}$  thickness as an extreme case. The corresponding TPEF images at three laser peak powers are reported in Fig. 5(b). The exponential decrease of ballistic light that remains after passing through scattering bone requires a higher illumination laser power to maintain the TPEF signal level. Furthermore, the speckles resulting from the scattering and the broadening of the focus spot significantly reduce the quality of the images. For these reasons, at a thickness of  $60 \text{ }\mu\text{m}$ , which is comparable to the photon MFP ( $49 \text{ }\mu\text{m}$ ), the three rows of outer hair cells (OHCs), a single row of inner hair cells (IHCs), the tunnel of Corti (TC), and other cellular structures are clearly visible in the TPEF image at the minimum excitation power used. A higher excitation power did not improve the image quality but actually resulted in fluorophore bleaching and lowered the signal level. At a thickness of  $100 \text{ }\mu\text{m}$ , cellular structures are still identifiable in the TPEF image using a medium level excitation power, which improves with higher power. Through a thickness of  $250 \text{ }\mu\text{m}$ , a meaningful cellular level image only results from the highest excitation power used, albeit with significantly compromised image acuity and contrast. Given that the



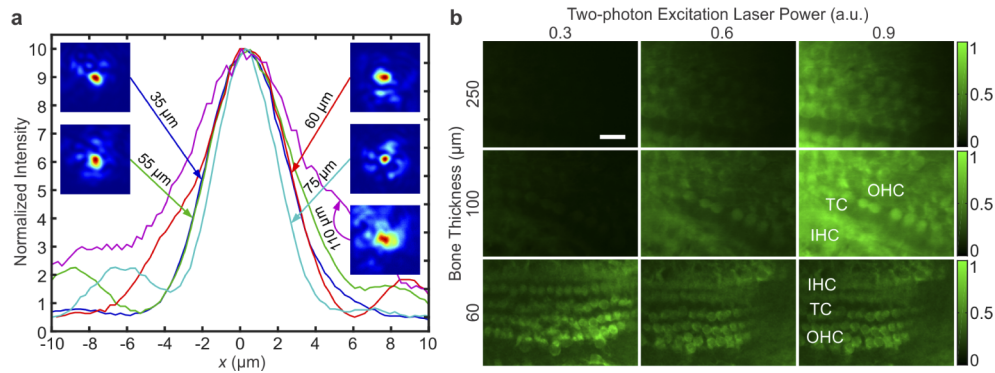


**Fig. 5.** Effects of bone thickness on the imaging through cochlear bone. **(a)** Distorted laser focus of 0.25 NA through different bone thicknesses. Curves are the intensity line profiles across the center of the focal spots normalized with the undistorted focus intensity. Insets show the corresponding images of the foci. **(b)** TPEF microscopy images in cochlear whole mounts through three bone thicknesses at three levels of excitation laser power. Mouse intracochlear structures are clearly visible through bone chips of 60  $\mu\text{m}$  and 100  $\mu\text{m}$  thickness. The images show signs of photobleaching at the thickness of 60  $\mu\text{m}$ , and reduced acuity and contrast at 100  $\mu\text{m}$  thickness. Images through a 250  $\mu\text{m}$  thick bone chip requires the highest excitation power used to reveal vaguely identifiable structures with a significantly compromised acuity and contrast. The excitation wavelength used was 785 nm, and the whole mounts were stained with Rhodamine 6G. IHC, inner hair cell. OHC, outer hair cell. TC, tunnel of Corti. Scale bars: 20  $\mu\text{m}$ .

intact mouse cochlear bone has a thickness of 200–300  $\mu\text{m}$  on average, our results suggest that thinning the bone down to 100  $\mu\text{m}$  via controlled ultrafast laser ablation is needed to reduce the effects of light scattering, which include signal loss and image blurring.

### 3.2. Intracochlear TPEF microscopy imaging in murine intact cochlea through laser-ablated bone

Our studies on the scattering properties of the cochlear bone (Fig. 4) and the effect of laser bone ablation on TPEF imaging of HCs in a cochlear whole mount through the bone (Fig. 5) provide the necessary parameters optimized for carrying out TPEF microscopy in the intact cochlea. Before the ablation, the cochlea was stained using phalloidin-488 for TPEF imaging (see Methods). We performed the ablation with the intact cochlea sample immersed in PBS in order to keep the sample hydrated, although the ablation objective was not immersed. This matches the conditions in the intended application because the middle ear, through which we will gain surgical access for cochlear bone ablation, is air-filled. The results are shown in Fig. 6. We focused on ablating the apical turn of the cochlea because in this region, the distance between HCs and the inner bony wall is small, measuring  $200 \pm 43$   $\mu\text{m}$ . We ablated a pattern area of  $500 \times 200$   $\mu\text{m}^2$  down to less than 40  $\mu\text{m}$  in thickness. Due to the curving nature of the cochlear chambers, the bone thickness after the ablation can vary by about 10  $\mu\text{m}$ . The control of laser parameters during ablation is crucial to avoid bone cracking while thinning it. The cochlear wall and interior were monitored with BF camera and OCT before (Figs. 6(a) and 6(b)) and after the ablation (Figs. 6(c) and 6(d)).

After the ablation, we transferred the phalloidin-488 stained sample to the commercial multiphoton microscope and obtained TPEF images of intracochlear cells through the ablated bone in the intact cochlea. The TPEF microscope collects the fluorescence image stack in epi mode as the laser focus scans down into the cochlea. Frames from the z-stack reveal intracochlear

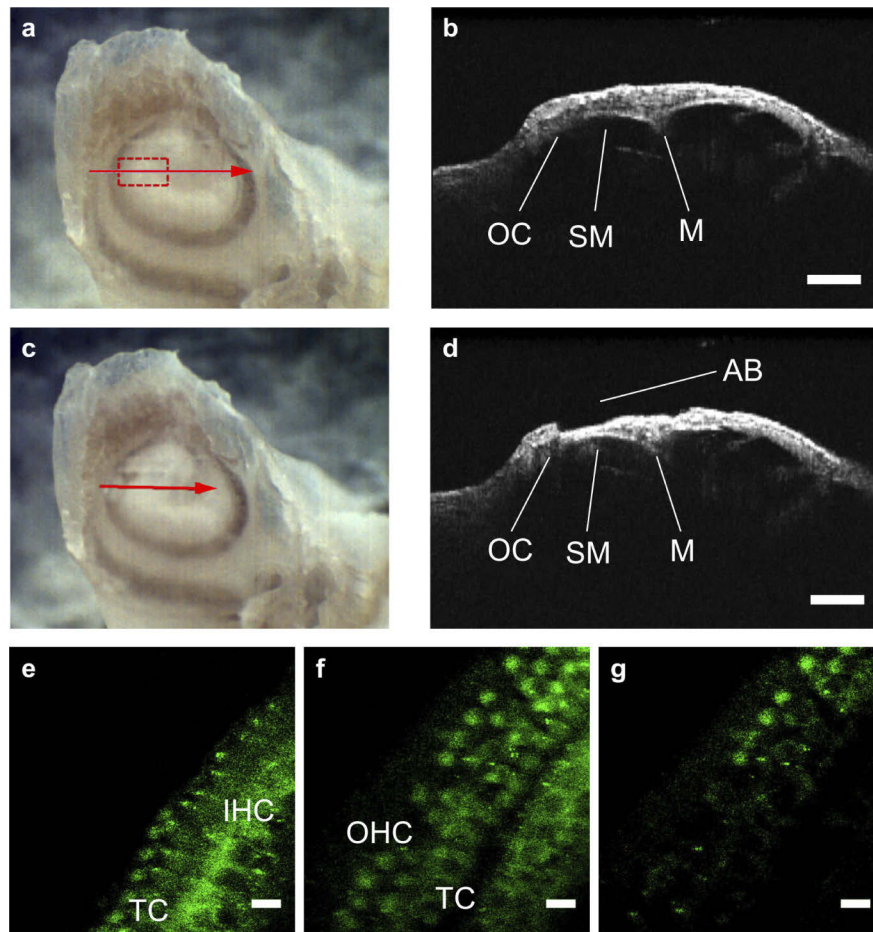


**Fig. 6.** Intracochlear hair cell imaging in intact murine cochlea through laser-ablated bone. (a) The BF image of the 3D intact cochlea before the ablation. Red dashed rectangle indicates the ablation area. (b) Cross-sectional OCT image acquired along the red arrow line in (a). (c) The BF image of the 3D intact cochlea before the ablation. (d) Cross-sectional OCT image acquired along the red arrow line in (c). Scale bars: 100  $\mu\text{m}$ . (e) (f) (g) Three TPEF microscopy images acquired while focusing from the external ablated cochlear surface to the region of the organ of Corti, revealing intracochlear cells and anatomic details. Hair cells were stained with Phalloidin 488. AB, apical bone. OC, organ of Corti. SM, scala media. M, interscalar septum. IHC, inner hair cell. OHC, outer hair cell. TC, tunnel of Corti. Scale bars: 10  $\mu\text{m}$ .

structures with high resolution 300  $\mu\text{m}$  behind the bone layer, such as the IHCs, the TC (Fig. 3(e)), the OHCs (Fig. 6(f)) and the supporting tissues (Fig. 6(g)). The Supplementary Media shows the whole TPEF z-stack starting from the external ablated bone surface, passing through the spiral ligament and stria vascularis layer and reaching the region of the OC.

#### 4. Discussion

According to Vogel et al. [44], the dominant mechanism of tissue disruption by tightly focused femtosecond pulses for repetition rates up to  $\sim 1$  MHz is plasma-mediated nanocavitation, while the dominant mechanism for repetition rates much greater than 1 MHz is free-electron induced

chemical decomposition. As the present work involves a laser repetition rate of 5 kHz, the ablation mechanism is clearly plasma-mediated nanocavitation.

Plasma-mediated laser ablation is known to generate a strong shockwave due to plasma expansion [45,46], which may raise a concern about damage in the hair cells given their close proximity to the ablation zone. To address this concern, we consider an earlier study [45] under similar experimental conditions (350 fs 1053 nm laser ablation at  $5.7 \text{ J cm}^{-2}$  fluence) in a collagen gel. A transient peak recoil pressure of 66 MPa, without an obvious rarefaction phase, that lasted about 50 ns (full width half maximum) at the ablation zone was measured in that study. In our experiment, the plasma-induced shock wave should have a comparable pressure profile, which roughly corresponds to a pulsed ultrasound of 10 MHz frequency at a repetition rate of 5 kHz and a duty factor of  $5 \times 10^{-4}$ . A major difference between this plasma-induced shock wave and a regular ultrasound wave is the lack of a rarefaction phase, which is the actual cause for cavitation and tissue damage. The effective wavelength of the shock wave is  $150 \mu\text{m}$  in water, assuming a sound speed of  $1500 \text{ m s}^{-1}$ . Given the ablation zone of approximately  $10 \mu\text{m}$  in diameter, which is much smaller than the ultrasound wavelength, the propagation of the shock wave is omnidirectional. Therefore, the transient peak pressure that an organ of Corti would sustain, which is assumed to be  $100 \mu\text{m}$  away from the ablation zone for a conservative estimation, is nearly 0.66 MPa following an inverse square law and ignoring any wave attenuation. This pressure is compression-only rather than alternating (compression-rarefaction) and is only a fraction of the rarefactional pressure limit in diagnostic ultrasound devices. The time-averaged acoustic power is approximately  $9.3 \mu\text{W}$ , assuming 100% of laser energy at the highest ablation fluence ( $3.7 \mu\text{J}$ ) used here is converted into acoustic energy in the shock wave for a conservative estimate. This corresponds to an acoustic intensity of  $7.4 \text{ mW cm}^{-2}$  at a distance  $100 \mu\text{m}$  away from the ablation zone, which is again a fraction of what is used in diagnostic ultrasound devices.

More quantitatively, the International Electrotechnical Commission (IEC) defined two non-dimensional indices as the standard measures to determine the potential for tissue damage by an ultrasound system [47]. The ultrasound-induced mechanical stress in the tissue is assessed with  $MI = P_r / C_{MI} \sqrt{f}$ , where  $P_r$  is the peak rarefaction pressure in MPa,  $f$  is the ultrasound frequency in MHz, and  $C_{MI} = 1 \text{ MPa MHz}^{-1/2}$  is a non-dimensionalization coefficient. For medical ultrasound devices, the Food and Drug Administration (FDA) requires that  $MI < 1.9$  in all tissues except the eyes where  $MI < 0.23$  is required [48]. The risk is considered negligible when  $MI < 0.5$  [49]. The ultrasound-induced tissue heating is measured with  $TI = W_p / C_{TI}$ , where  $W_p$  is the time-averaged acoustic power, and  $C_{TI} = 210 \text{ mW MHz}$  is the coefficient for soft tissue. It is deemed a negligible risk for values of  $TI < 1$ . Due to the difference between the laser-induced shock wave and diagnostic ultrasound, accurate calculation of the indices is not available, and we can only make a worst-case estimate of the damage potential. To estimate  $MI$ , we assume a rarefaction phase does occur in the shock wave with an amplitude equal to that of the compression phase. This results in  $MI = 0.21$ , which suggests that the risk of hair cell damage due to mechanical stress is negligible. The actual  $MI$  is much lower due to the lack of a rarefaction phase. For  $TI$ , we assume that the entire time-averaged acoustic power of  $9.3 \mu\text{W}$  resulting from the laser pulse acts on the organ of Corti, which gives  $TI = 4 \times 10^{-4}$  and indicates that the tissue heating is negligible. We therefore conclude that the hair cells at least  $100 \mu\text{m}$  away from the ablation zone are safe from the laser-induced shocks. This is well in line with the findings in a recent initial study [50] on the effects of high frequency ultrasound (40 MHz at an amplitude of 1.24 MPa and an intensity of  $157 \text{ mW cm}^{-2}$ ) in hair cells. Further reduction of the shock wave pressure can be achieved by using an objective of a higher NA in the ablation, which requires lower pulse energy to attain the needed fluence owing to the smaller focus spot.

The above analyses may appear questionable at first sight because they are based on experimental data in a collagen gel while the cochlear bone is a hard tissue. At the femto- to picosecond timescale, however, plasma and shock wave physics in condensed matter becomes similar in

different materials. Right after the passage of the ultrashort laser pulse, the energy density of the plasma, and consequently the initial pressure of the shock wave it creates shortly after, can be estimated through [51]  $\varepsilon = (3/2)n_{cr}\Delta E$ , where  $n_{cr}$  is the critical electron density of the plasma at the ablation laser frequency, and  $\Delta E$  is the electronic band gap. In soft tissues where water is a major constituent, the band gap when treated as an amorphous semiconductor is represented by the water band gap of 6.5 eV [52]. On the other hand, in bones where hydroxyapatite makes up roughly 70% of the mass, the band gap is dominated by that of hydroxyapatite, which is 7.3 eV based on a quantum calculation [53]. Therefore, the initial shock wave pressure in bones is only approximately 12% higher than that in soft tissues.

Despite the non-thermal nature of femtosecond laser ablation, the elevated temperature in the target zone due to the average laser energy flux must be taken into consideration. It was shown [54,55] that an air or water flow during the ablation significantly reduces the thermal deposition and improves the efficiency. However, at the level of laser power (15 mW maximum) and volume rate of ablation (no more than  $0.05 \text{ mm}^3 \text{ min}^{-1}$ ) in the intended applications, we expect the thermal effects to be rather mild. A previous study using similar parameters (700 fs 1053 nm laser ablation at 10  $\mu\text{J}$  pulse energy and 10 kHz repetition rate) showed that the temperature rise is below  $2^\circ\text{C}$  on the opposite surface of the ablation in a 1-mm thick porcine otic capsule sample, which is linearly proportional to the ablation pulse energy. Projecting this temperature change to our parameters (3.7  $\mu\text{J}$  maximum pulse energy at 5 kHz repetition rate), we estimate that the temperature rise in our work is approximately  $0.4^\circ\text{C}$ . This is well below the  $3^\circ\text{C}$  tolerance found in rabbit cochlea [56]. Therefore, and also in light of the increased infection risks and the complicated drainage requirements, we do not use a cooling flow in this study and in the intended applications.

Like many other biological tissues, bones generally demonstrate a highly anisotropic scattering [41,57], and the angular distribution of the scattered light approximately follows the Henyey-Greenstein phase function. The scattering anisotropy is quantified with the anisotropy factor  $g = \langle \cos \theta \rangle$ , which represents the mean cosine of the scattering angle  $\theta$  of all photons after one scattering in a turbid medium. It is often greater than 0.9 in many biological tissues. A reduced scattering coefficient is defined as  $\mu'_s = (1 - g)\mu_s$  which leads to a large transport MFP,  $\ell_T = 1/\mu'_s$ , within which light only suffers mostly low-angle deflections and follows a snaky path. Light focusing and imaging is generally considered achievable without special efforts to unscramble the light passing through a scattering medium whose thickness is below a few  $\ell_T$ . However, in the cochlear bone, one of the densest bones in the body,  $\langle \cos \theta \rangle$  rapidly decreases with the thickness [40] due to multiple scattering and becomes only 0.4 at the thickness of 120  $\mu\text{m}$ . This results in a significantly broadened laser focus compared with the ballistic photon focus beyond a few photon MFP, as revealed in our PSF measurements. Therefore, to preserve as much information as possible in the images of the small cochlear sensorineural cells, it is of a great advantage to thin the cochlear bone down to one or two photon MFP, i.e. 50–100  $\mu\text{m}$ .

Although optical clearing of bone has been applied *in vivo* [58,59] to reduce bone scattering through decalcification and refractive index matching for deeper light penetration, a number of potential problems present obstacles in its application to the inner ear. The main concern is that chemicals used for bone clearing can be toxic to the delicate sensorineural structures within the cochlea. In addition, bone clearing can cause tissue dehydration [58] and structural changes in the collagen [60], which plays an essential role in the elasticity and rigidity of the structures that sustain cochlear function. In comparison, our bone ablation approach, which is highly localized to a volume of no more than 500  $\mu\text{m}$  in each dimension, is not ototoxic. Moreover, the small windows of ablated bone can be filled with removable, precisely fashioned bone plugs of the same structural integrity to prevent any adverse long-term effects on cochlear function.

Our technique points to a new possibility in answering the challenge of cellular-level imaging in the inner ear by creating optical windows in the bony cage through laser microsurgery. However,



further studies are essential before this technique can be translated into a clinical diagnostic tool. In particular, future research should focus on the parameter optimization to accommodate individual physiological differences, and on the utilization of the intrinsic fluorescence from the cochlear sensorineural cells [61,62] rather than exogenous fluorescent dyes.

## 5. Conclusion

We have demonstrated a technique for imaging cells behind a strongly scattering medium (bone) by thinning the bone using monitored femtosecond laser ablation. In both extracted OCs and intact whole cochleae, precise laser ablation can efficiently reduce the bone thickness to a level where the scattering in the remaining bone no longer hinders the TPEF imaging of intracochlear structures behind it, including IHCs and OHCs, with high resolution. Thinning the bone to one or two photon MFP provides best image quality. Our approach offers significant imaging flexibility because the ablation sites can be strategically placed along the cochlear length to interrogate cochlear regions encoding specific acoustic frequencies. Our methodology naturally suits a fiber-based endoscopic implementation that integrates capabilities of both ultrafast laser ablation [63,64] and TPEF imaging [65,66].

## Funding

Fondation Bertarelli (10271).

## Acknowledgements

The authors would like to acknowledge Donald Conkey for his support in the optical setup for laser ablation and Thomas Lanvin for his helpful assistance in the Labview programming software. We also thank Shelley Batts for her guidance in mouse cochlear dissections. K.M.S. and D.P. conceived the project. M.R. conducted the experiments. Y.P. and M.R. analyzed the results and wrote the manuscript. All authors critically reviewed and edited the manuscript.

## Disclosures

The authors declare no conflicts of interest.

## References

1. C. L. Hsieh, Y. Pu, R. Grange, and D. Psaltis, "Digital phase conjugation of second harmonic radiation emitted by nanoparticles in turbid media," *Opt. Express* **18**(12), 12283–12290 (2010).
2. A. P. Mosk, A. Lagendijk, G. Lerosey, and M. Fink, "Controlling waves in space and time for imaging and focusing in complex media," *Nat. Photonics* **6**(5), 283–292 (2012).
3. I. M. Vellekoop and A. P. Mosk, "Focusing coherent light through opaque strongly scattering media," *Opt. Lett.* **32**(16), 2309–2311 (2007).
4. C. L. Hsieh, Y. Pu, R. Grange, G. Laporte, and D. Psaltis, "Imaging through turbid layers by scanning the phase conjugated second harmonic radiation from a nanoparticle," *Opt. Express* **18**(20), 20723–20731 (2010).
5. X. Yang, C. L. Hsieh, Y. Pu, and D. Psaltis, "Three-dimensional scanning microscopy through thin turbid media," *Opt. Express* **20**(3), 2500–2506 (2012).
6. S. C. Feng, C. Kane, P. A. Lee, and A. D. Stone, "Correlations and fluctuations of coherent wave transmission through disordered media," *Phys. Rev. Lett.* **61**(7), 834–837 (1988).
7. E. Papagiakoumou, A. Begue, B. Leshem, O. Schwartz, B. M. Stell, J. Bradley, D. Oron, and V. Emiliani, "Functional patterned multiphoton excitation deep inside scattering tissue," *Nat. Photonics* **7**(4), 274–278 (2013).
8. J. H. Park, W. Sun, and M. Cui, "High-resolution in vivo imaging of mouse brain through the intact skull," *Proc. Natl. Acad. Sci. U. S. A.* **112**(30), 9236–9241 (2015).
9. S. Popoff, G. Lerosey, M. Fink, A. C. Boccara, and S. Gigan, "Image transmission through an opaque material," *Nat. Commun.* **1**(1), 81 (2010).
10. P. J. Drew, A. Y. Shih, J. D. Driscoll, P. M. Knutsen, P. Blinder, D. Davalos, K. Akassoglou, P. S. Tsai, and D. Kleinfeld, "Chronic optical access through a polished and reinforced thinned skull," *Nat. Methods* **7**(12), 981–984 (2010).



11. G. Yang, F. Pan, C. N. Parkhurst, J. Grutzendler, and W. B. Gan, "Thinned-skull cranial window technique for long-term imaging of the cortex in live mice," *Nat. Protoc.* **5**(2), 201–208 (2010).
12. X. Liu, D. Du, and G. Mourou, "Laser ablation and micromachining with ultrashort laser pulses," *IEEE J. Quantum Electron.* **33**(10), 1706–1716 (1997).
13. C. L. Hoy, O. Ferhanoglu, M. Yildirim, K. H. Kim, S. S. Karajanagi, K. M. C. Chan, J. B. Kobler, S. M. Zeitel, and A. Ben-Yakar, "Clinical ultrafast laser surgery: Recent advances and future directions," *IEEE J. Sel. Top. Quantum Electron.* **20**(2), 14 (2014).
14. S. A. Boppart, J. Herrmann, C. Pitris, D. L. Stamper, M. E. Brezinski, and J. G. Fujimoto, "High-resolution optical coherence tomography-guided laser ablation of surgical tissue," *J. Surg. Res.* **82**(2), 275–284 (1999).
15. O. Kermani, W. Fabian, and H. Lubatschowski, "Real-time optical coherence tomography-guided femtosecond laser sub-bowman keratomileusis on human donor eyes," *Am. J. Ophthalmol.* **146**(1), 42–45 (2008).
16. D. C. Jeong, P. S. Tsai, and D. Kleinfeld, "All-optical osteotomy to create windows for transcranial imaging in mice," *Opt. Express* **21**(20), 23160–23168 (2013).
17. Y. Raphael, "Cochlear pathology, sensory cell death and regeneration," *Br. Med. Bull.* **63**(1), 25–38 (2002).
18. J. E. Sagers, L. D. Landegger, S. Worthington, J. B. Nadol, and K. M. Stankovic, "Human cochlear histopathology reflects clinical signatures of primary neural degeneration," *Sci. Rep.* **7**(1), 4884 (2017).
19. K. Kawamoto, S. H. Sha, R. Minoda, M. Izumikawa, H. Kuriyama, J. Schacht, and Y. Raphael, "Antioxidant gene therapy can protect hearing and hair cells from ototoxicity," *Mol. Ther.* **9**(2), 173–181 (2004).
20. K. Kawamoto, M. Yagi, T. Stover, S. Kanzaki, and Y. Raphael, "Hearing and hair cells are protected by adenoviral gene therapy with *tgf-beta 1* and *gdnf*," *Mol. Ther.* **7**(4), 484–492 (2003).
21. Y. Ren, L. D. Landegger, and K. M. Stankovic, "Gene therapy for human sensorineural hearing loss," *Front. Cell. Neurosci.* **13**, 323 (2019).
22. T. Okano and M. W. Kelley, "Stem cell therapy for the inner ear: Recent advances and future directions," *Trends Amplif.* **16**(1), 4–18 (2012).
23. N. H. Cho, J. H. Jang, W. Jung, and J. Kim, "In vivo imaging of middle-ear and inner-ear microstructures of a mouse guided by sd-oct combined with a surgical microscope," *Opt. Express* **22**(8), 8985–8995 (2014).
24. H. Y. Lee, P. D. Raphael, J. Park, A. K. Ellerbee, B. E. Applegate, and J. S. Oghalai, "Noninvasive in vivo imaging reveals differences between tectorial membrane and basilar membrane traveling waves in the mouse cochlea," *Proc. Natl. Acad. Sci. U. S. A.* **112**(10), 3128–3133 (2015).
25. J. S. Iyer, S. A. Batts, K. K. Chu, M. I. Sahin, H. M. Leung, G. J. Tearney, and K. M. Stankovic, "Micro-optical coherence tomography of the mammalian cochlea," *Sci. Rep.* **6**(1), 10 (2016).
26. M. Risoud, J. Sircoglou, G. Dedieu, M. Tardivel, C. Vincent, and N. X. Bonne, "Imaging and cell count in cleared intact cochlea in the mongolian gerbil using laser scanning confocal microscopy," *Eur. Ann. Otorhinolaryngol.-Head Neck Dis.* **134**(4), 221–224 (2017).
27. L. Nolte, N. Tinne, J. Schulze, D. Heinemann, G. C. Antonopoulos, H. Meyer, H. G. Nothwang, T. Lenarz, A. Heisterkamp, A. Warnecke, and T. Ripken, "Scanning laser optical tomography for in toto imaging of the murine cochlea," *PLoS One* **12**(4), 10 (2017).
28. G. H. MacDonald and E. W. Rubel, "Three-dimensional imaging of the intact mouse cochlea by fluorescent laser scanning confocal microscopy," *Hear. Res.* **243**(1–2), 1–10 (2008).
29. J. S. Iyer, N. Zhu, S. Gasilov, H. M. Ladak, S. K. Agrawal, and K. M. Stankovic, "Visualizing the 3D cytoarchitecture of the human cochlea in an intact temporal bone using synchrotron radiation phase contrast imaging," *Biomed. Opt. Express* **9**(8), 3757–3767 (2018).
30. F. Spoor and F. Zonneveld, "Comparative review of the human bony labyrinth," in *Yearbook of Physical Anthropology, vol 41*, C. Ruff, ed. (Wiley-Liss, Inc, 1998), pp. 211–251.
31. S. K. Yoo, G. Wang, J. T. Rubinstein, and M. W. Vannier, "Three-dimensional geometric modeling of the cochlea using helico-spiral approximation," *IEEE Trans. Biomed. Eng.* **47**(10), 1392–1402 (2000).
32. A. A. Poznyakovskiy, T. Zahnert, Y. Kalaidzidis, R. Schmidt, B. Fischer, J. Baumgart, and Y. M. Yarin, "The creation of geometric three-dimensional models of the inner ear based on micro computer tomography data," *Hear. Res.* **243**(1–2), 95–104 (2008).
33. F. Y. Chen, N. Choudhury, J. F. Zheng, S. Matthews, A. L. Nutall, and S. L. Jacques, "In vivo imaging and low-coherence interferometry of organ of corti vibration," *J. Biomed. Opt.* **12**(2), 021006 (2007).
34. W. Denk, J. H. Strickler, and W. W. Webb, "Two-photon laser scanning fluorescence microscopy," *Science* **248**(4951), 73–76 (1990).
35. X. Yang, Y. Pu, C. L. Hsieh, C. A. Ong, D. Psaltis, and K. M. Stankovic, "Two-photon microscopy of the mouse cochlea in situ for cellular diagnosis," *J. Biomed. Opt.* **18**(3), 031104 (2012).
36. S. Nyberg, N. J. Abbott, X. R. Shi, P. S. Steyger, and A. Dabdoub, "Delivery of therapeutics to the inner ear: The challenge of the blood-labyrinth barrier," *Sci. Transl. Med.* **11**(482), eaao0935 (2019).
37. L. T. Canguero, R. Vilar, A. M. B. do Rego, and V. S. F. Muralha, "Femtosecond laser ablation of bovine cortical bone," *J. Biomed. Opt.* **17**(12), 125005 (2012).
38. B. Girard, D. Yu, M. R. Armstrong, B. C. Wilson, C. M. L. Clokie, and R. J. D. Miller, "Effects of femtosecond laser irradiation on osseous tissues," *Lasers Surg. Med.* **39**(3), 273–285 (2007).
39. L. J. Mortensen, C. Alt, R. Turcotte, M. Masek, T. M. Liu, D. C. Cote, C. Xu, G. Intini, and C. P. Lin, "Femtosecond laser bone ablation with a high repetition rate fiber laser source," *Biomed. Opt. Express* **6**(1), 32–42 (2015).

40. A. O. Ugnell and P. A. Oberg, "The optical properties of the cochlear bone," *Med. Eng. Phys.* **19**(7), 630–636 (1997).
41. M. Firbank, M. Hiraoka, M. Essenpreis, and D. T. Delpy, "Measurement of the optical-properties of the skull in the wavelength range 650–950 nm," *Phys. Med. Biol.* **38**(4), 503–510 (1993).
42. N. Ugryumova, S. J. Matcher, and D. P. Attenburrow, "Measurement of bone mineral density via light scattering," *Phys. Med. Biol.* **49**(3), 469–483 (2004).
43. K. M. Yoo and R. R. Alfano, "Time-resolved coherent and incoherent components of forward light-scattering in random-media," *Opt. Lett.* **15**(6), 320–322 (1990).
44. A. Vogel, J. Noack, G. Huttman, and G. Paltauf, "Mechanisms of femtosecond laser nanosurgery of cells and tissues," *Appl. Phys. B: Lasers Opt.* **81**(8), 1015–1047 (2005).
45. A. A. Oraevsky, L. B. DaSilva, A. M. Rubenchik, M. D. Feit, M. E. Glinsky, M. D. Perry, B. M. Mammini, W. Small, and B. C. Stuart, "Plasma mediated ablation of biological tissues with nanosecond-to-femtosecond laser pulses: Relative role of linear and nonlinear absorption," *IEEE J. Sel. Top. Quantum Electron.* **2**(4), 801–809 (1996).
46. T. Juhasz, G. A. Kastis, C. Suarez, Z. Bor, and W. E. Bron, "Time-resolved observations of shock waves and cavitation bubbles generated by femtosecond laser pulses in corneal tissue and water," *Lasers Surg. Med.* **19**(1), 23–31 (1996).
47. International Electrotechnical Commission, IEC 62359:2010, "Ultrasonics - field characterization - test methods for the determination of thermal and mechanical indices related to medical diagnostic ultrasonic fields" (2010).
48. "Information for manufacturers seeking marketing clearance of diagnostic ultrasound systems and transducers," Food and Drug Administration, ed. (2008).
49. R. S. C. Cobbold, *Foundations of Biomedical Ultrasound* (Oxford University Press, 2007).
50. T. G. Landry, M. L. Bance, R. B. Adamson, and J. A. Brown, "No effect of prolonged pulsed high frequency ultrasound imaging of the basilar membrane on cochlear function or hair cell survival found in an initial study," *Hear. Res.* **363**, 28–38 (2018).
51. J. Noack and A. Vogel, "Laser-induced plasma formation in water at nanosecond to femtosecond time scales: Calculation of thresholds, absorption coefficients, and energy density," *IEEE J. Quantum Electron.* **35**(8), 1156–1167 (1999).
52. F. Williams, S. P. Varma, and S. Hillenius, "Liquid water as a lone-pair amorphous-semiconductor," *J. Chem. Phys.* **64**(4), 1549–1554 (1976).
53. L. A. Avakyan, E. V. Paramonova, J. Coutinho, S. Oberg, V. S. Bystrov, and L. A. Bugaev, "Optoelectronics and defect levels in hydroxyapatite by first-principles," *J. Chem. Phys.* **148**(15), 154706 (2018).
54. L. T. Canguero and R. Vilar, "Influence of the pulse frequency and water cooling on the femtosecond laser ablation of bovine cortical bone," *Appl. Surf. Sci.* **283**, 1012–1017 (2013).
55. W. J. Li, J. Q. Zheng, Y. P. Zhang, F. S. Yuan, and P. J. Lyu, "Temperature and depth evaluation of the in vitro effects of femtosecond laser on oral soft tissue, with or without air-cooling," *Lasers Med. Sci.* **34**(4), 649–658 (2019).
56. W. S. Noyes, T. V. McCaffrey, D. A. Fabry, M. S. Robinette, and V. J. Suman, "Effect of temperature elevation on rabbit cochlear function as measured by distortion-product otoacoustic emissions," *Otolaryngol. Head Neck Surg.* **115**(6), 548–552 (1996).
57. S. L. Jacques, "Optical properties of biological tissues: A review," *Phys. Med. Biol.* **58**(11), R37–R61 (2013).
58. D. Zhu, K. V. Larin, Q. M. Luo, and V. V. Tuchin, "Recent progress in tissue optical clearing," *Laser Photonics Rev.* **7**(5), 732–757 (2013).
59. Y. J. Zhao, T. T. Yu, C. Zhang, Z. Li, Q. M. Luo, T. H. Xu, and D. Zhu, "Skull optical clearing window for in vivo imaging of the mouse cortex at synaptic resolution," *Light: Sci. Appl.* **7**(1), 9 (2018).
60. V. V. Tuchin, "Optical clearing of tissues and blood using the immersion method," *J. Phys. D: Appl. Phys.* **38**(15), 2497–2518 (2005).
61. L. M. Tiede, S. M. Rocha-Sanchez, R. Hallworth, M. G. Nichols, and K. Beisel, "Determination of hair cell metabolic state in isolated cochlear preparations by two-photon microscopy," *J. Biomed. Opt.* **12**(2), 021004 (2007).
62. X. Yang, Y. Pu, D. Psaltis, and K. M. Stankovic, "In situ imaging of the mouse cochlea using two-photon microscopy," in *Optical Methods for Inspection, Characterization, and Imaging of Biomaterials*, P. Ferraro, M. RitschMarte, S. Grilli, and D. Stifter, eds. (SPIE-Int Soc Optical Engineering, 2013).
63. O. Ferhanoglu, M. Yildirim, K. Subramanian, and A. Ben-Yakar, "A 5-mm piezo-scanning fiber device for high speed ultrafast laser microsurgery," *Biomed. Opt. Express* **5**(7), 2023–2036 (2014).
64. E. Kakkava, M. Romito, D. B. Conkey, D. Loterie, K. M. Stankovic, C. Moser, and D. Psaltis, "Selective femtosecond laser ablation via two-photon fluorescence imaging through a multimode fiber," *Biomed. Opt. Express* **10**(2), 423–433 (2019).
65. D. B. Conkey, N. Stasio, E. E. Morales-Delgado, M. Romito, C. Moser, and D. Psaltis, "Lensless two-photon imaging through a multicore fiber with coherence-gated digital phase conjugation," *J. Biomed. Opt.* **21**(4), 045002 (2016).
66. E. E. Morales-Delgado, D. Psaltis, and C. Moser, "Two-photon imaging through a multimode fiber," *Opt. Express* **23**(25), 32158–32170 (2015).